Supporting Information for the article

"Interpreting the cause of bound earthquakes at underground injection experiments"

by

Ryan Schultz, Linus Villiger, Valentin Gischig, & Stefan Wiemer

published in

Solid Earth

Contents of this file

Supplementary Text

S1: Stage drop-out test at PNR-1z

Here, we perform a perturbation analysis to better understand how the EW-test responds to poorly-resolved cases. To do so, we start with the PNR-1z dataset and perform the EW-test using data from all the stages as a single cluster. We then omit the first stage from the cluster of earthquakes and then perform the EW-test again. This drop-out process is sequentially repeated until only the last stage is left. This perturbation is the same as those already presented in this manuscript, and similar to those from prior studies (Schultz et al., 2025).

We plot a smoothed version of this analysis (Figure S16). This analysis indicates that the best resolved cluster is (unsurprisingly) the one that includes all stage information, with a best-fit *n*-exponent of ~1.6. As initial stages sequentially drop-out, the confidence in the cluster being bound generally decreases and the *n*-exponent also decreases. Eventually enough data is removed such that we fall below the thresholds for statistical confidence and an *n*-exponent of 0.5 is approached.

Generally, this observation supports our interpretation of bound-fractures and unbound-faults (Figure 13). In this drop-out analysis, omitting earlier stages would be expected to increasingly ignore the initial creation of the fracture network. In this sense, drop-out progressively emulates stimulation into a large pre-existing fracture network. Thus, an unbound response is expected in the limit of only considering the last stage – since there is already a large and extensive pre-existing fracture network for M_{LRG} events to grow into uninhibited. If enough drop-out stages are reincorporated back into the cluster, the response starts appearing tectonic-like (or X-like), since the (apparent) unbound growth eventually encounters an abrupt upper limit (and this limit is not well-resolved enough to sense its change with time). Next, an intermediate amount of drop-out would encounter this abrupt upper limit, and start to sense its change with time, but not well enough to accurately constrain the *n*-exponent. In the final limit, our data is well-resolved enough to accurately constrain the true *n*-exponent.

This highlights the importance of capturing the initial M_{LRG} events for accurate EW-test results for cases with volume-based M_{MAX}. Conversely, this also highlights a potential observational bias within the EW-test, regarding the accuracy of the *n*-exponent. Because of this, we favour the observational bias as the most likely explanation of the X-like *n*-exponent (Figure

15). We note that this observational bias will likely be relevant in realistic settings – such as for hydraulic fracturing stimulations starting in a perforated well. Potentially, this bias could be accounted for by including a y-intercept term to volume-based M_{MAX} relationships.

Supplementary Figures

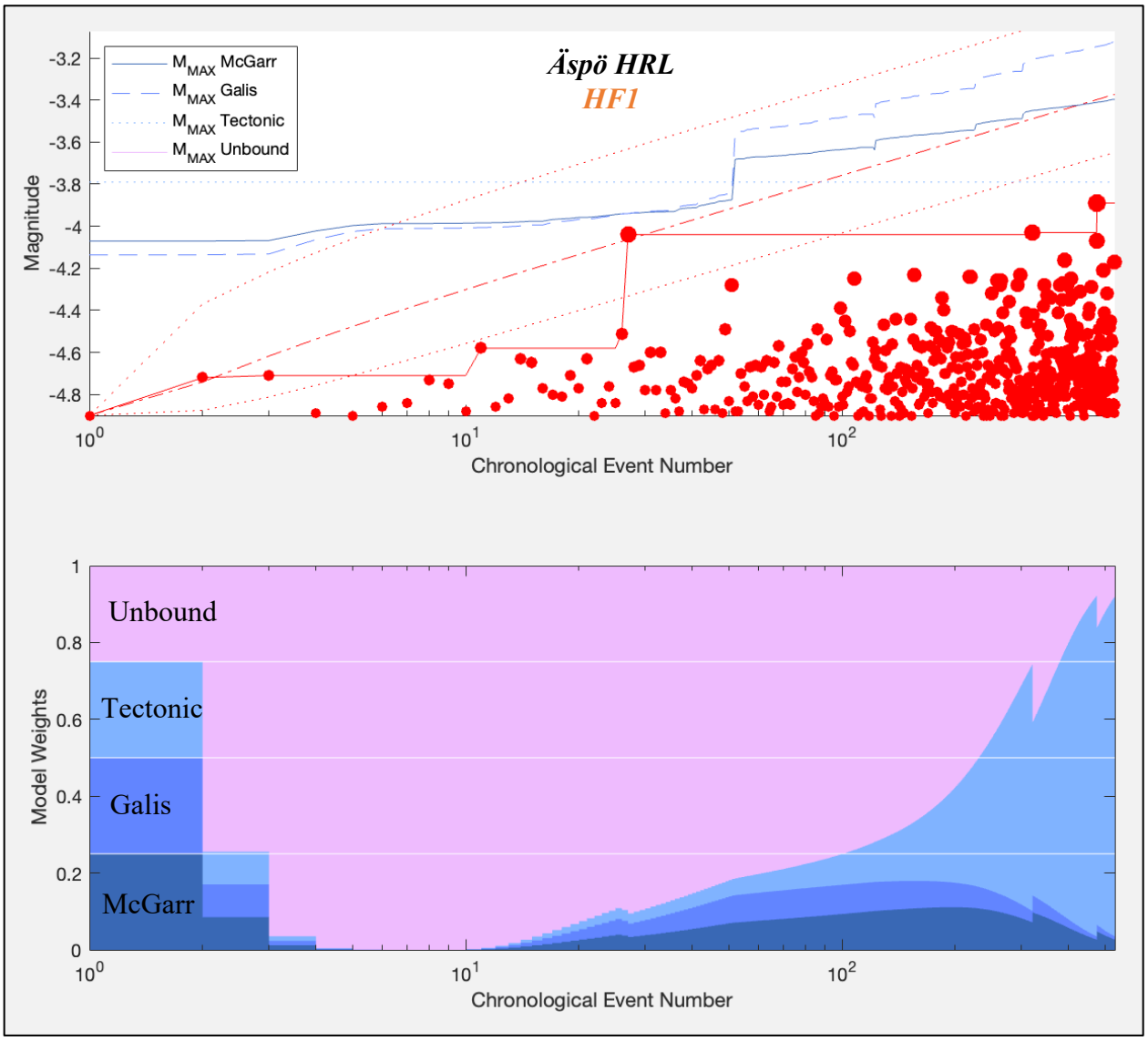

Figure S1. Using the EW-test to discern between M_{MAX} models for HF1 at the Äspö HRL. In the top panel, the catalogue of earthquake magnitudes (red circles) and the observed M_{LRG} sequence (red lines & circles), and expected M_{LRG} at the 10/50/90 percentiles (red dashed lines) are tested using three M_{MAX} assumptions (blue lines). In the bottom panel, AIC/BIC-based ensemble model weights (blue bars) using all data prior to each new M_{LRG} value are shown.

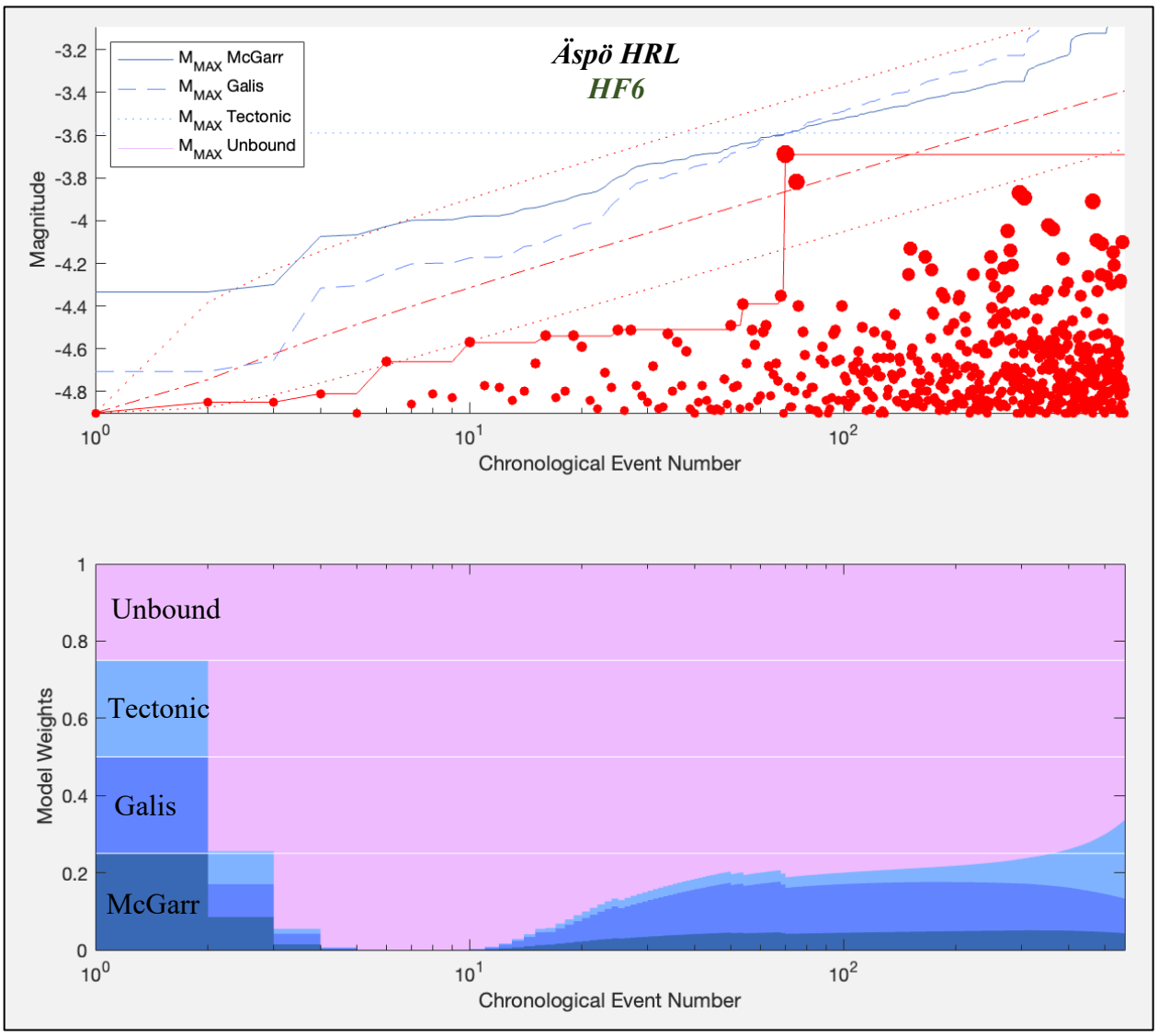

Figure S2. Using the EW-test to discern between M_{MAX} models for HF6 at the Äspö HRL. In the top panel, the catalogue of earthquake magnitudes (red circles), the observed M_{LRG} sequence (red lines & circles), and expected M_{LRG} at the 10/50/90 percentiles (red dashed lines) are tested using three M_{MAX} assumptions (blue lines). In the bottom panel, AIC/BIC-based ensemble model weights (coloured bars) using all data prior to each new event are shown.

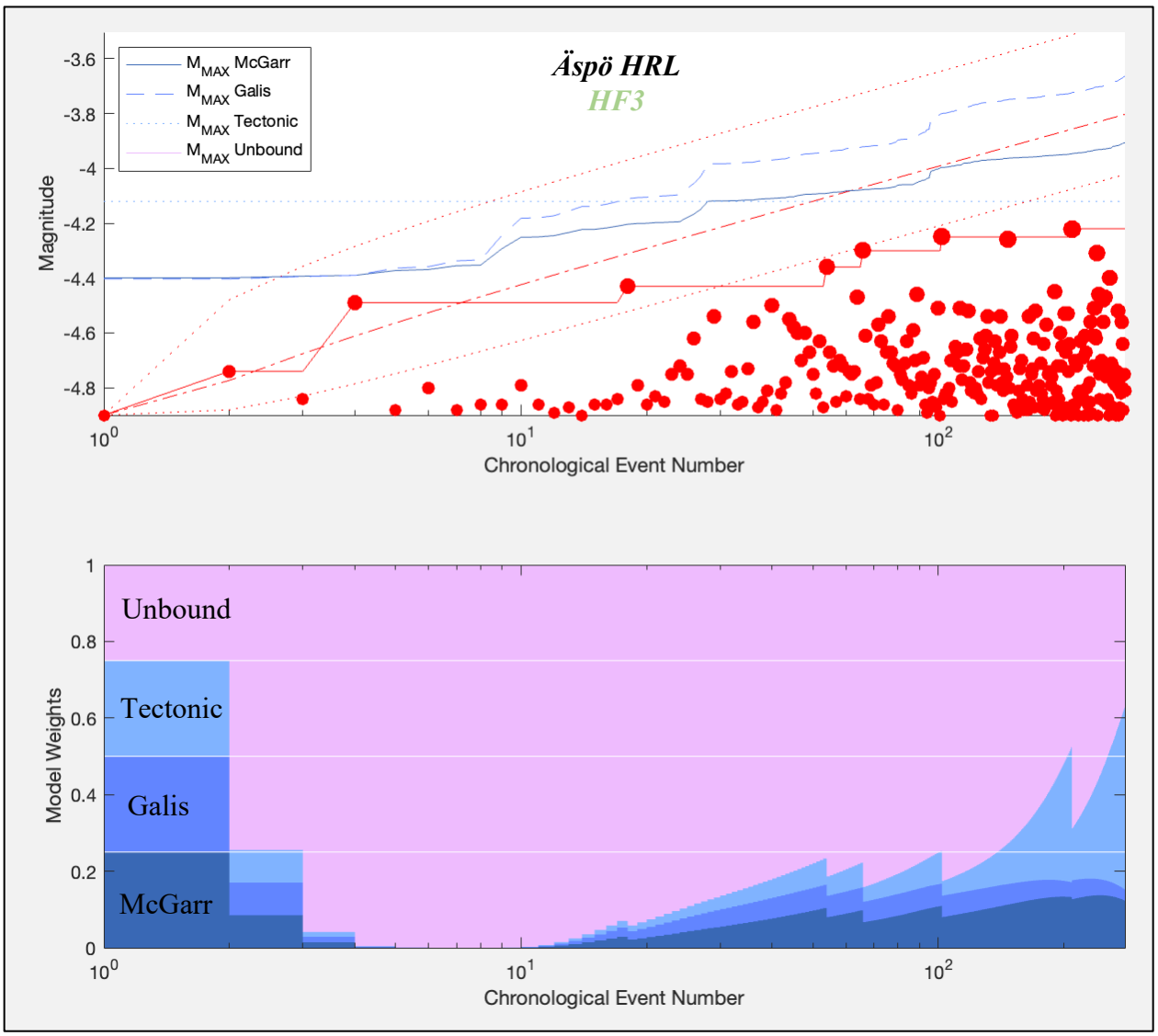

Figure S3. Using the EW-test to discern between M_{MAX} models for HF3 at the Äspö HRL. In the top panel, the catalogue of earthquake magnitudes (red circles), the observed M_{LRG} sequence (red lines & circles), and expected M_{LRG} at the 10/50/90 percentiles (red dashed lines) are tested using three M_{MAX} assumptions (blue lines). In the bottom panel, AIC/BIC-based ensemble model weights (coloured bars) using all data prior to each new event are shown.

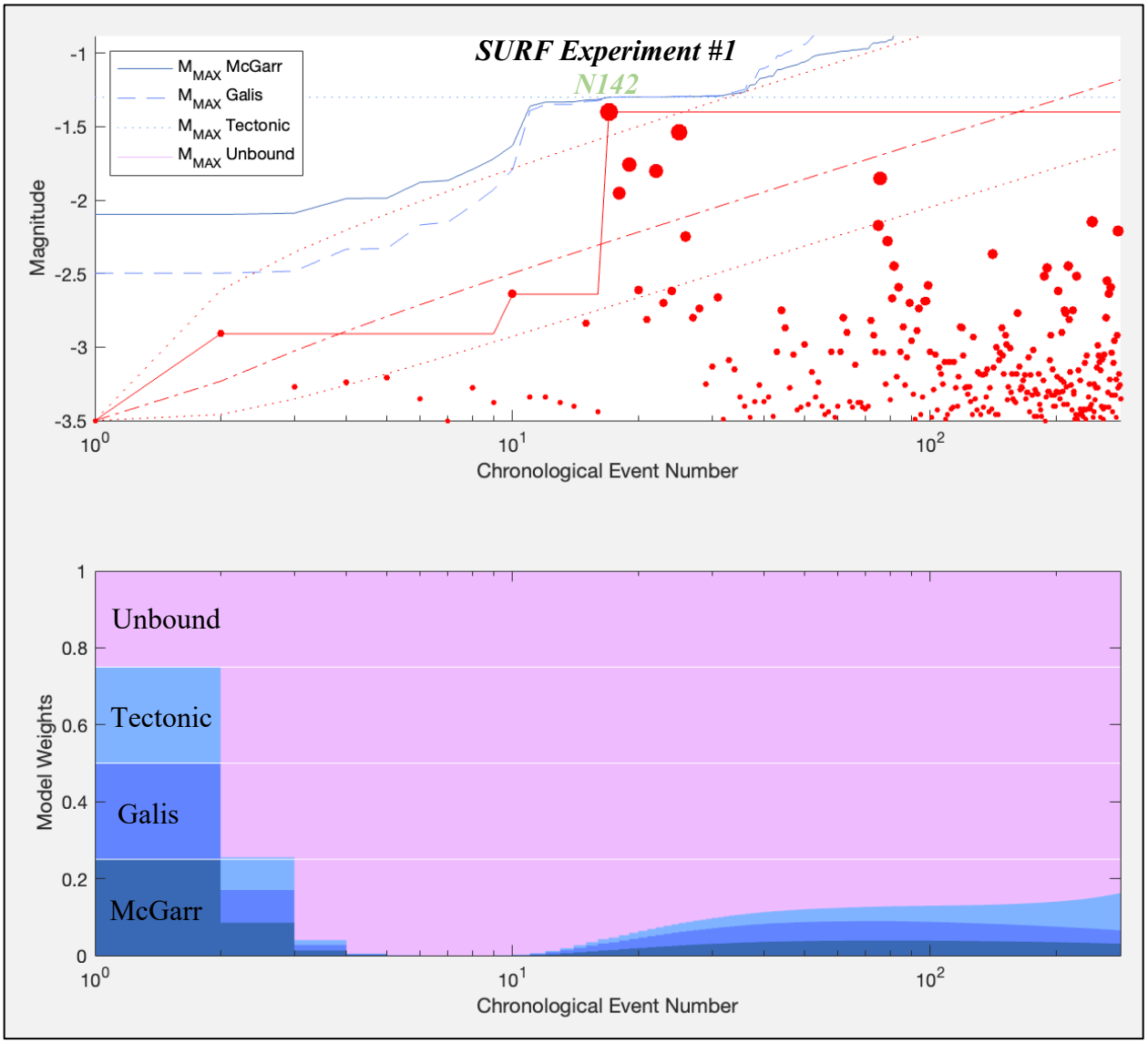

Figure S4. Using the EW-test to discern between M_{MAX} models for N142 at SURF Experiment #1. In the top panel, the catalogue of earthquake magnitudes (red circles), the observed M_{LRG} sequence (red lines & circles), and expected M_{LRG} at the 10/50/90 percentiles (red dashed lines) are tested using three M_{MAX} assumptions (blue lines). In the bottom panel, AIC/BIC-based ensemble model weights (coloured bars) using all data prior to each new event are shown.

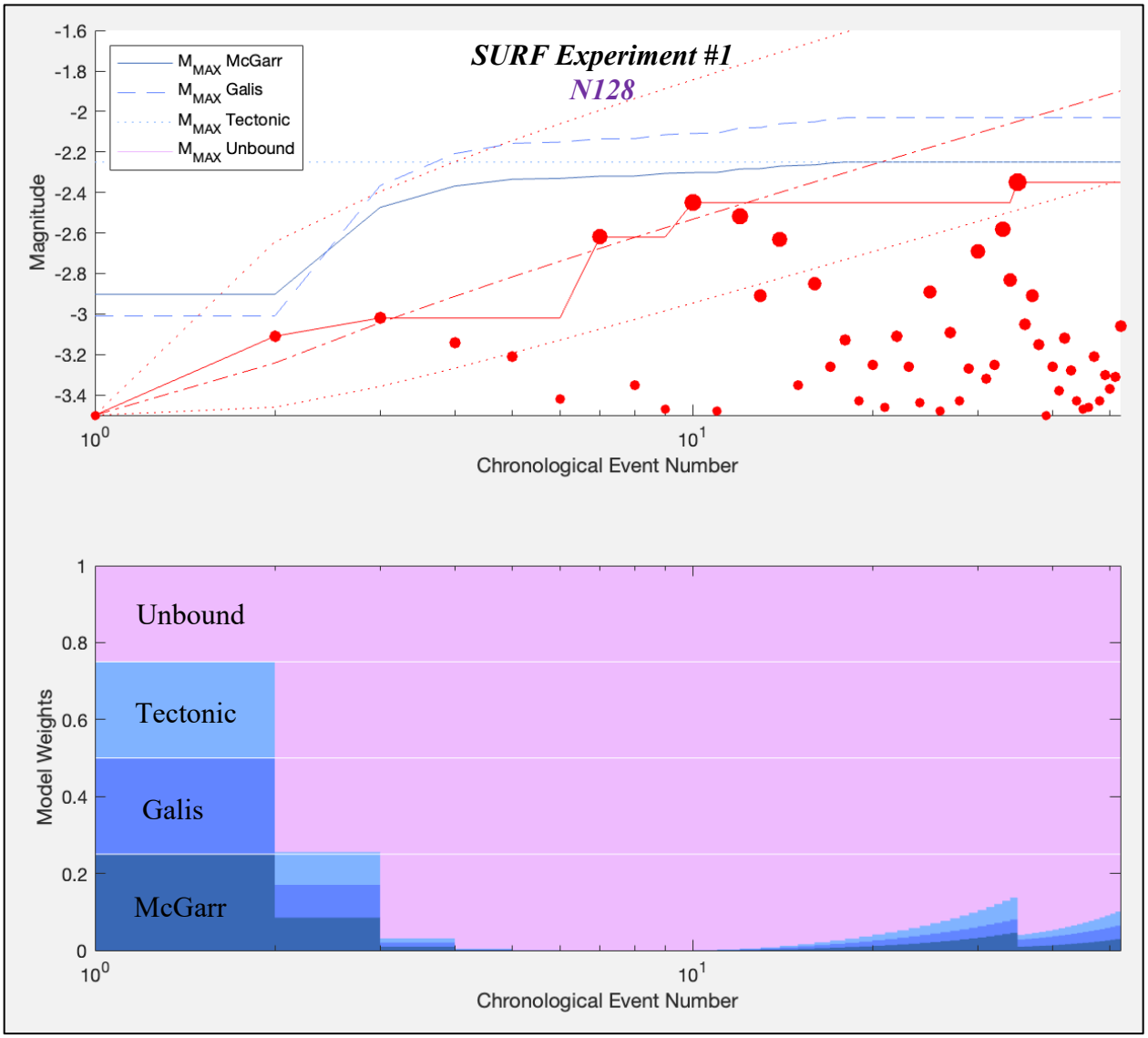

Figure S5. Using the EW-test to discern between M_{MAX} models for N128 at SURF Experiment #1. In the top panel, the catalogue of earthquake magnitudes (red circles), the observed M_{LRG} sequence (red lines & circles), and expected M_{LRG} at the 10/50/90 percentiles (red dashed lines) are tested using three M_{MAX} assumptions (blue lines). In the bottom panel, AIC/BIC-based ensemble model weights (coloured bars) using all data prior to each new event are shown.

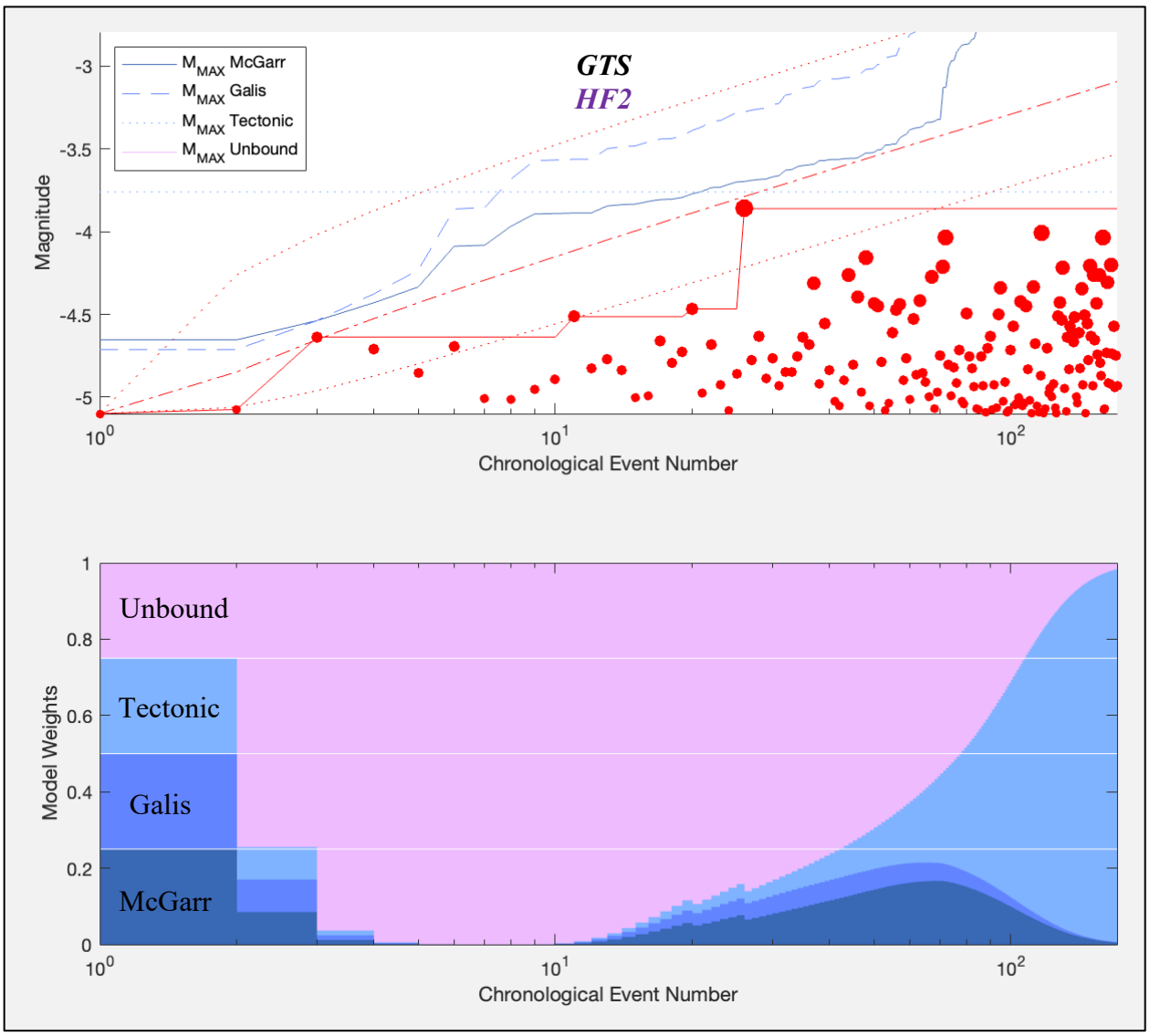

Figure S6. Using the EW-test to discern between M_{MAX} models for HF2 at the GTS. In the top panel, the catalogue of earthquake magnitudes (red circles), the observed M_{LRG} sequence (red lines & circles), and expected M_{LRG} at the 10/50/90 percentiles (red dashed lines) are tested using three M_{MAX} assumptions (blue lines). In the bottom panel, AIC/BIC-based ensemble model weights (coloured bars) using all data prior to each new event are shown.

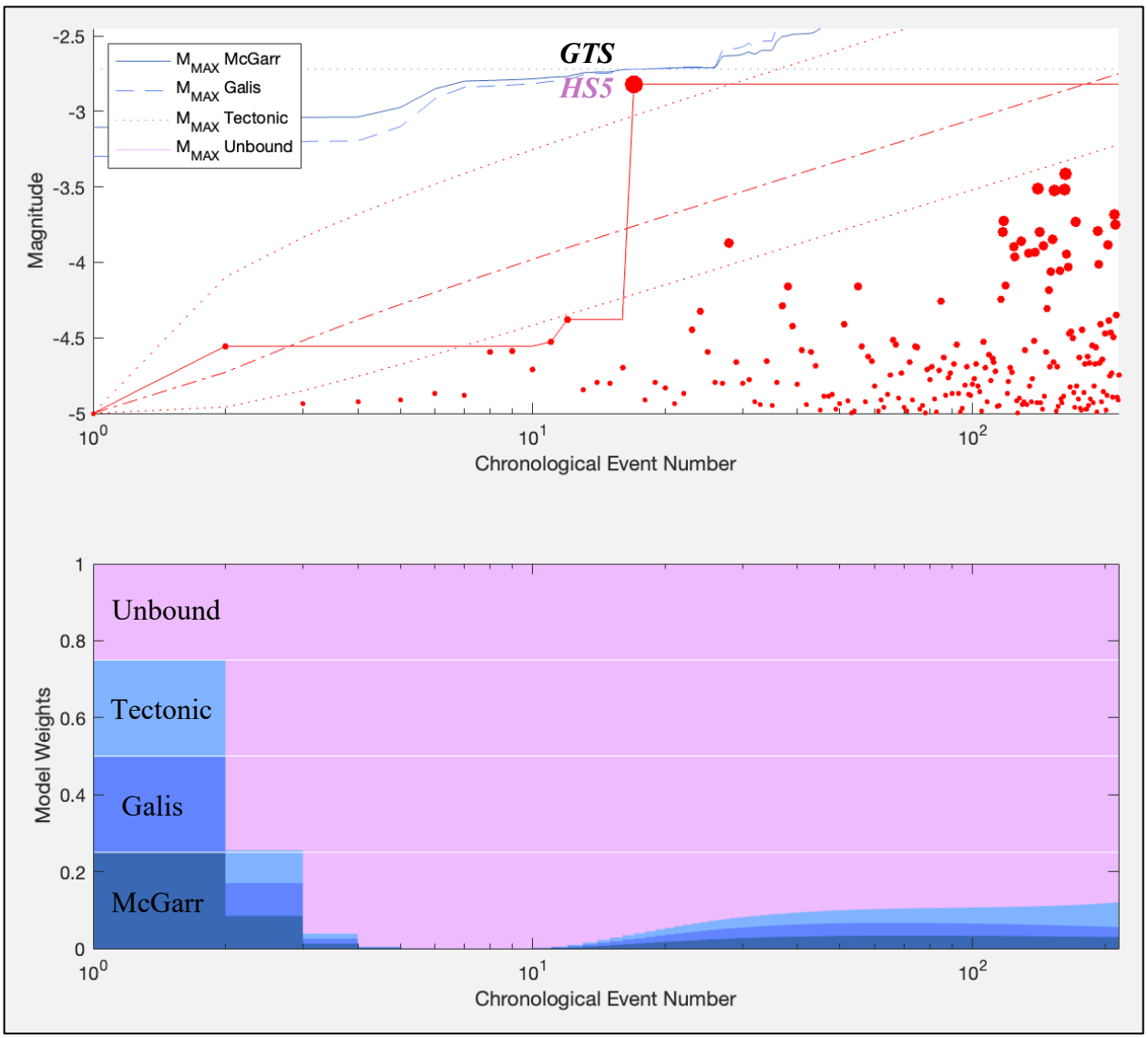

Figure S7. Using the EW-test to discern between M_{MAX} models for HS5 at the GTS. In the top panel, the catalogue of earthquake magnitudes (red circles), the observed M_{LRG} sequence (red lines & circles), and expected M_{LRG} at the 10/50/90 percentiles (red dashed lines) are tested using three M_{MAX} assumptions (blue lines). In the bottom panel, AIC/BIC-based ensemble model weights (coloured bars) using all data prior to each new event are shown.

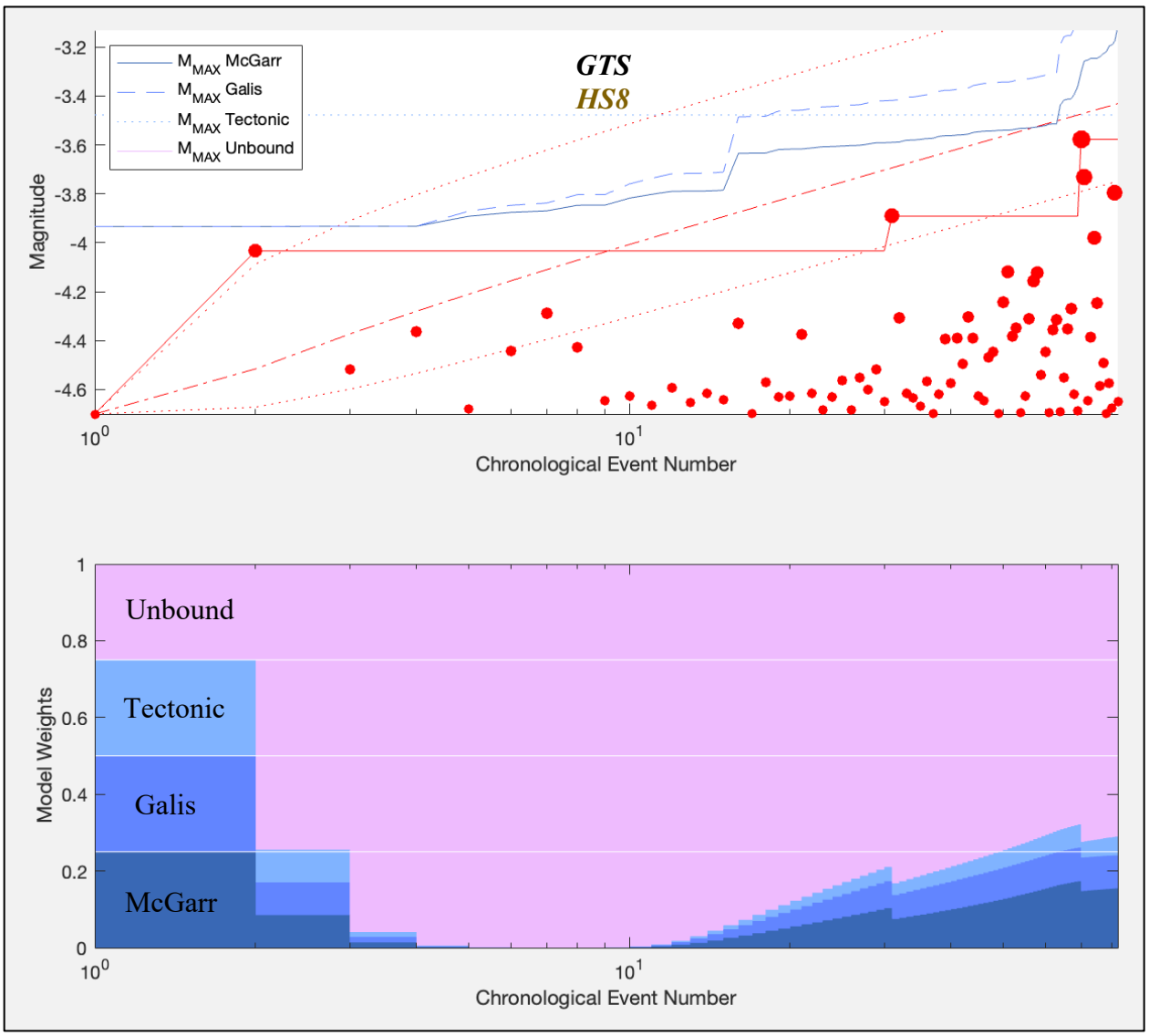

Figure S8. Using the EW-test to discern between M_{MAX} models for HS8 at the GTS. In the top panel, the catalogue of earthquake magnitudes (red circles), the observed M_{LRG} sequence (red lines & circles), and expected M_{LRG} at the 10/50/90 percentiles (red dashed lines) are tested using three M_{MAX} assumptions (blue lines). In the bottom panel, AIC/BIC-based ensemble model weights (coloured bars) using all data prior to each new event are shown.

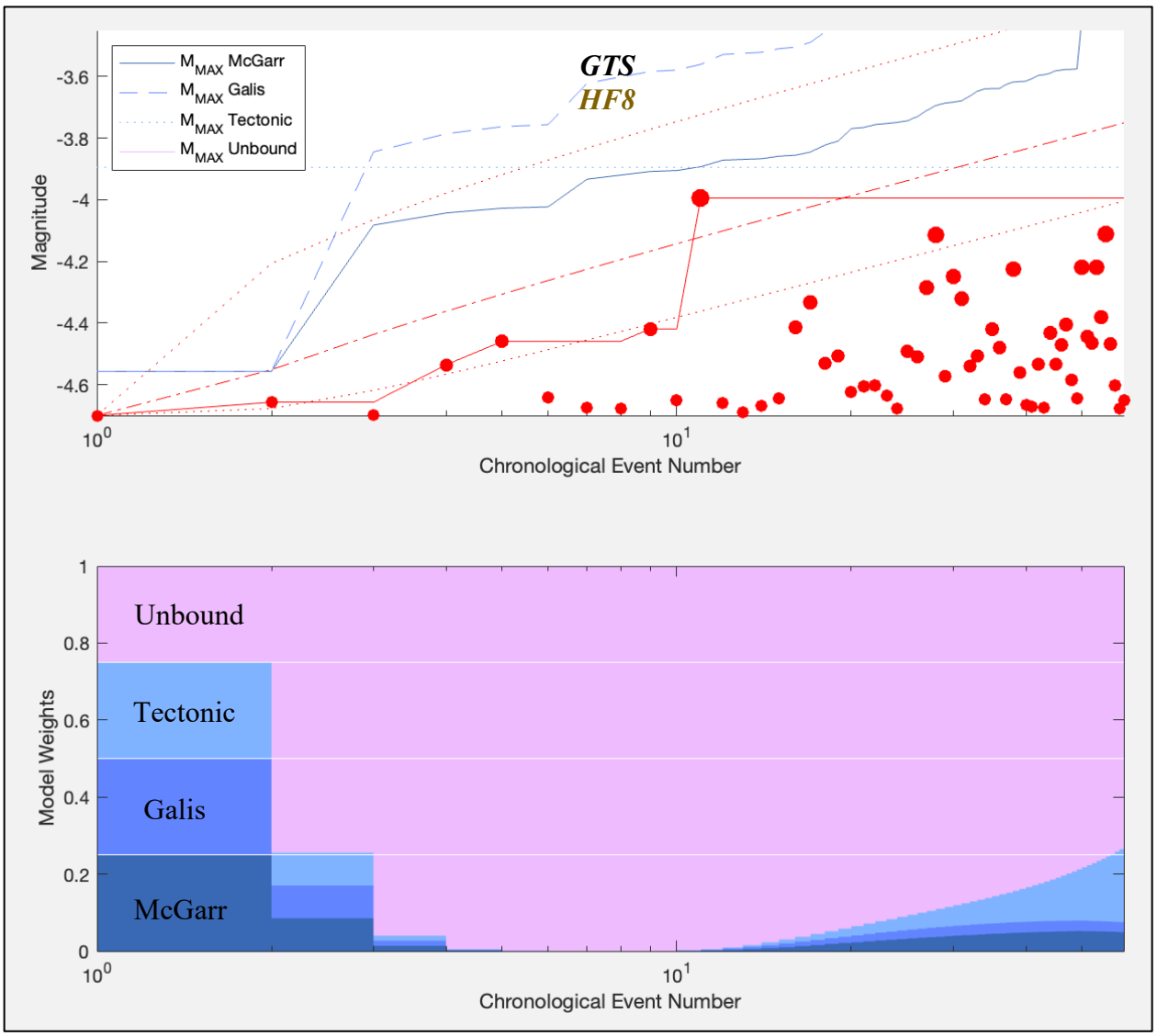

Figure S9. Using the EW-test to discern between M_{MAX} models for HF8 at the GTS. In the top panel, the catalogue of earthquake magnitudes (red circles), the observed M_{LRG} sequence (red lines & circles), and expected M_{LRG} at the 10/50/90 percentiles (red dashed lines) are tested using three M_{MAX} assumptions (blue lines). In the bottom panel, AIC/BIC-based ensemble model weights (coloured bars) using all data prior to each new event are shown.

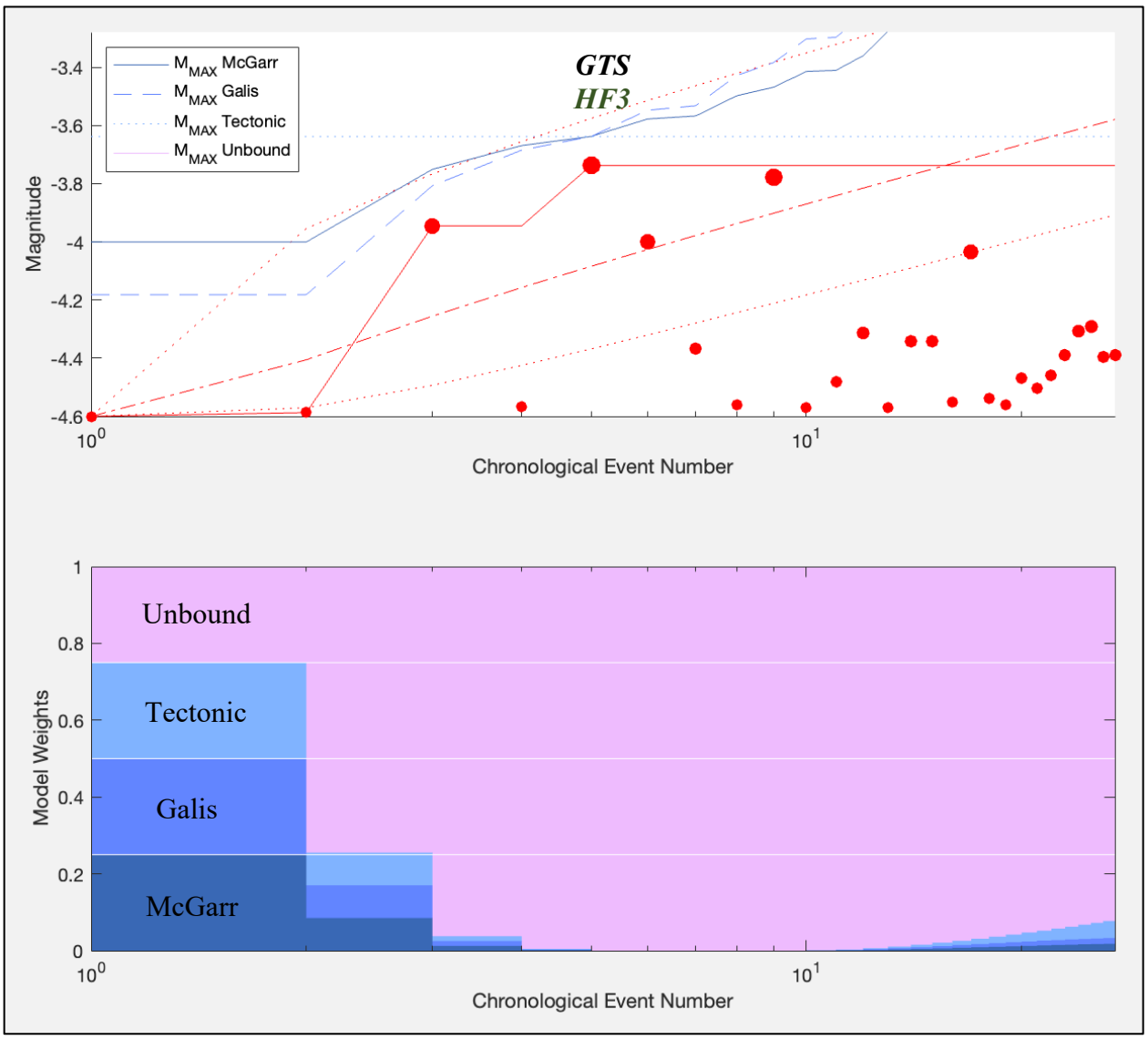

Figure S10. Using the EW-test to discern between M_{MAX} models for HF3 at the GTS. In the top panel, the catalogue of earthquake magnitudes (red circles), the observed M_{LRG} sequence (red lines & circles), and expected M_{LRG} at the 10/50/90 percentiles (red dashed lines) are tested using three M_{MAX} assumptions (blue lines). In the bottom panel, AIC/BIC-based ensemble model weights (coloured bars) using all data prior to each new event are shown.

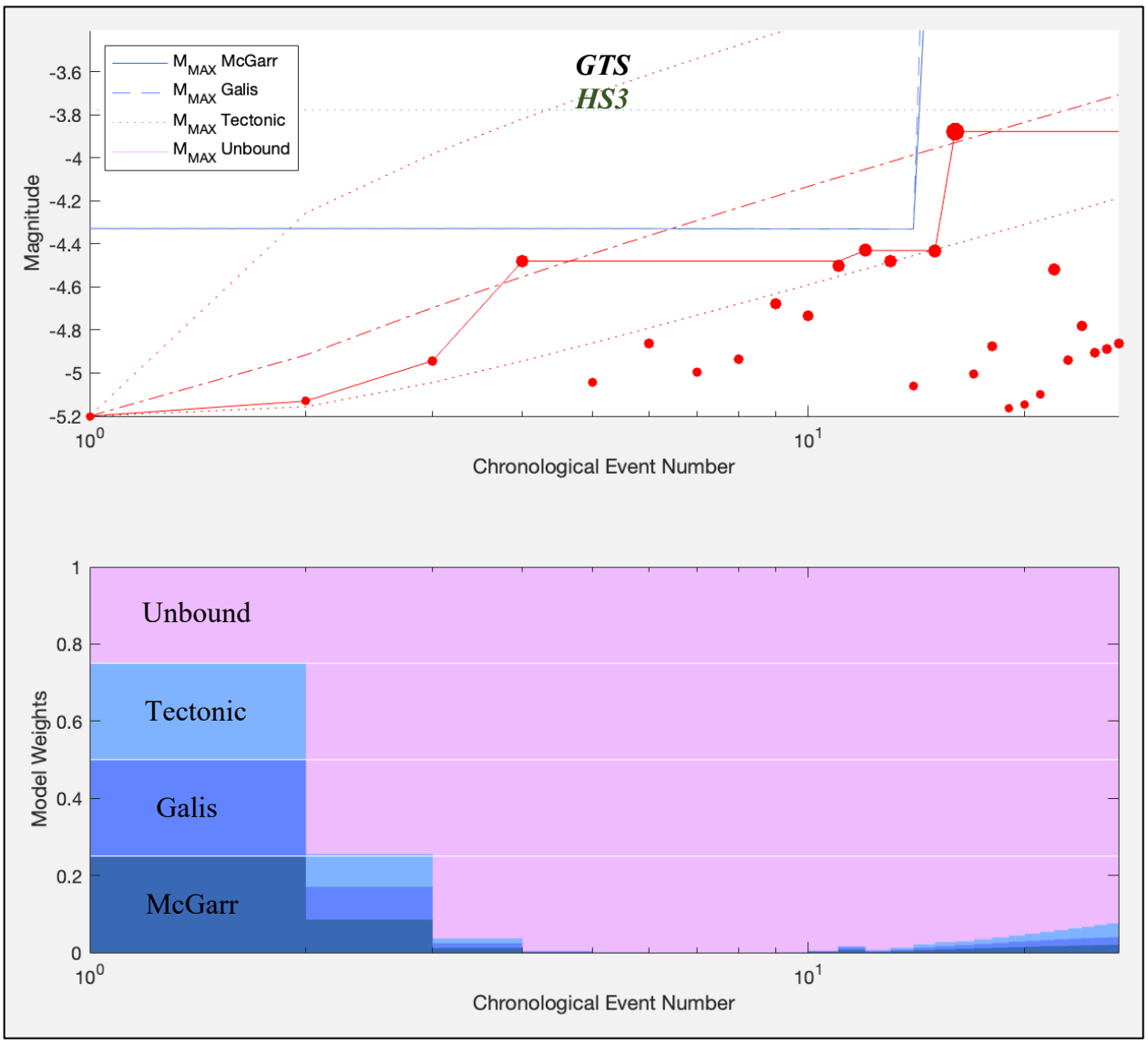

Figure S11. Using the EW-test to discern between M_{MAX} models for HS3 at the GTS. In the top panel, the catalogue of earthquake magnitudes (red circles), the observed M_{LRG} sequence (red lines & circles), and expected M_{LRG} at the 10/50/90 percentiles (red dashed lines) are tested using three M_{MAX} assumptions (blue lines). In the bottom panel, AIC/BIC-based ensemble model weights (coloured bars) using all data prior to each new event are shown.

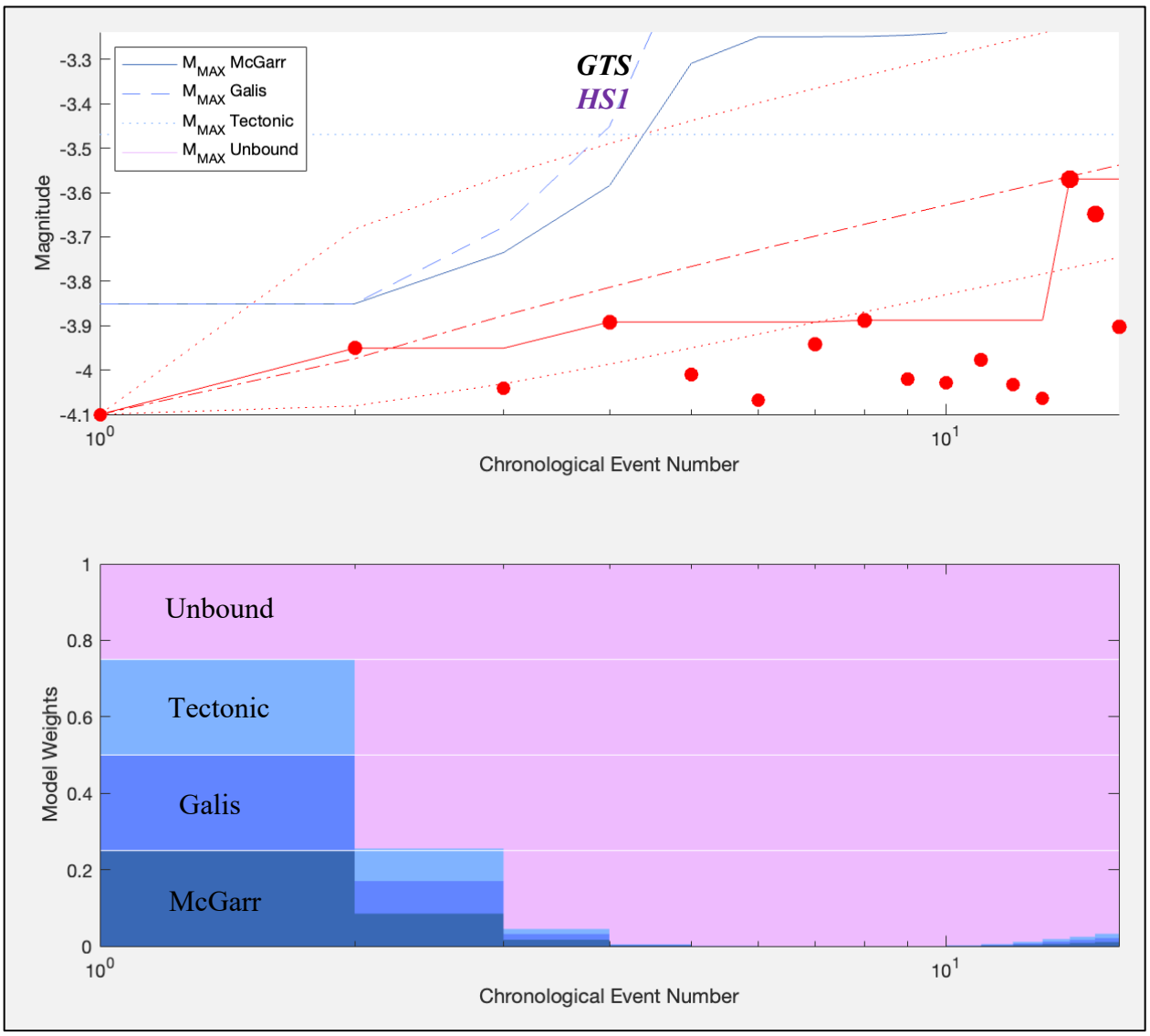

Figure S12. Using the EW-test to discern between M_{MAX} models for HS1 at the GTS In the top panel, the catalogue of earthquake magnitudes (red circles), the observed M_{LRG} sequence (red lines & circles), and expected M_{LRG} at the 10/50/90 percentiles (red dashed lines) are tested using three M_{MAX} assumptions (blue lines). In the bottom panel, AIC/BIC-based ensemble model weights (coloured bars) using all data prior to each new event are shown.

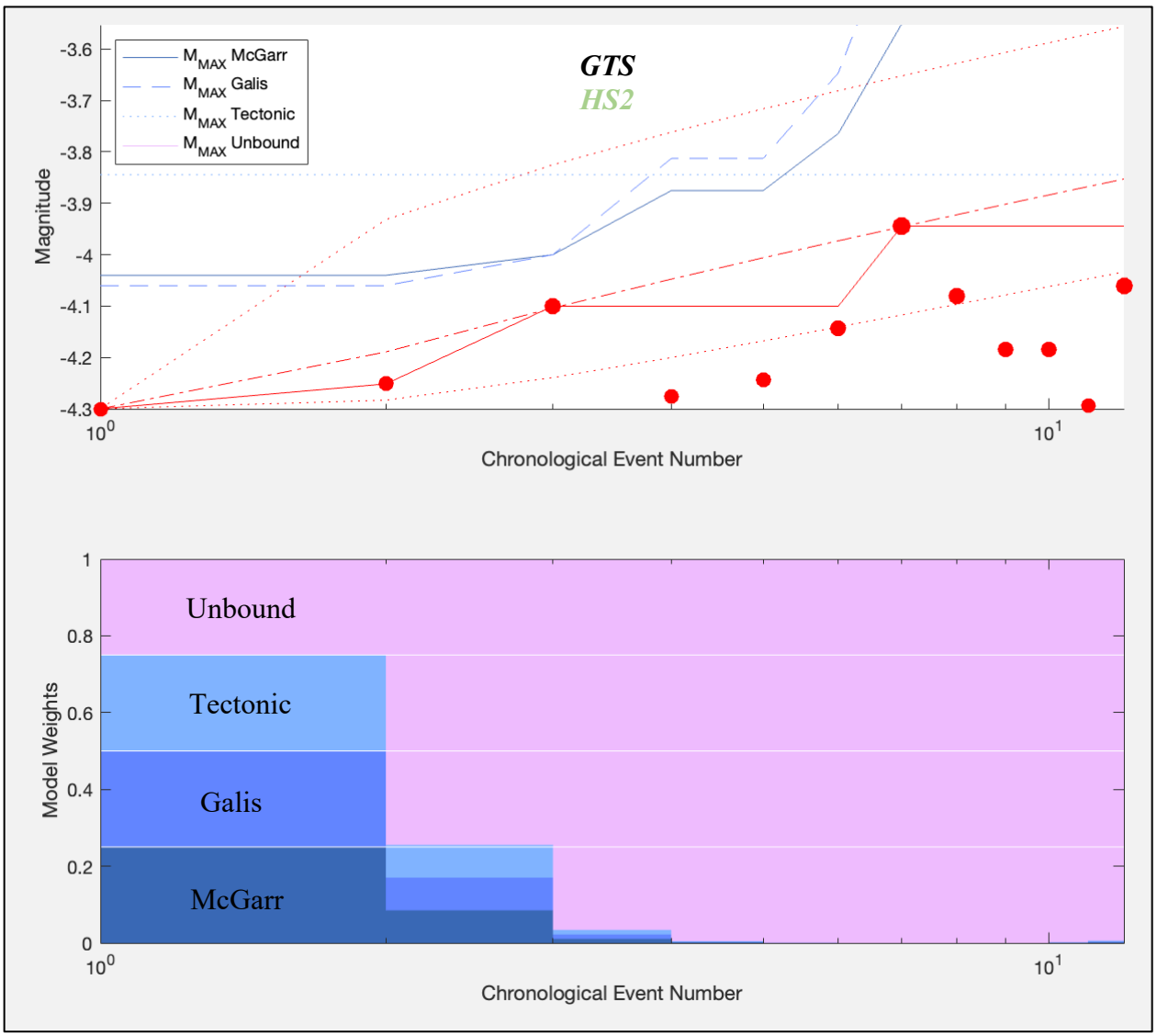

Figure S13. Using the EW-test to discern between M_{MAX} models for HS2 at the GTS. In the top panel, the catalogue of earthquake magnitudes (red circles), the observed M_{LRG} sequence (red lines & circles), and expected M_{LRG} at the 10/50/90 percentiles (red dashed lines) are tested using three M_{MAX} assumptions (blue lines). In the bottom panel, AIC/BIC-based ensemble model weights (coloured bars) using all data prior to each new event are shown.

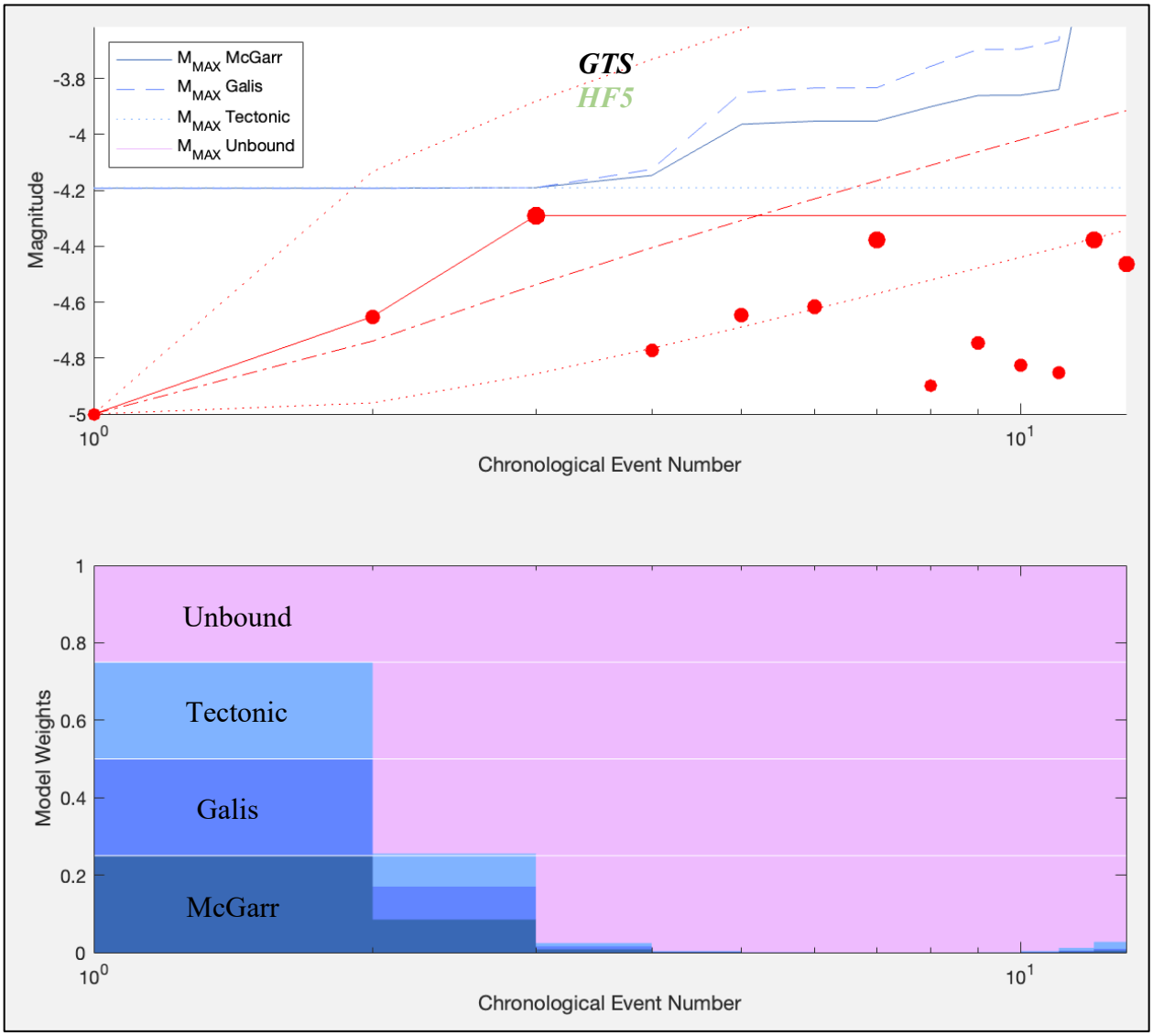

Figure S14. Using the EW-test to discern between M_{MAX} models for HF5 at the GTS. In the top panel, the catalogue of earthquake magnitudes (red circles), the observed M_{LRG} sequence (red lines & circles), and expected M_{LRG} at the 10/50/90 percentiles (red dashed lines) are tested using three M_{MAX} assumptions (blue lines). In the bottom panel, AIC/BIC-based ensemble model weights (coloured bars) using all data prior to each new event are shown.

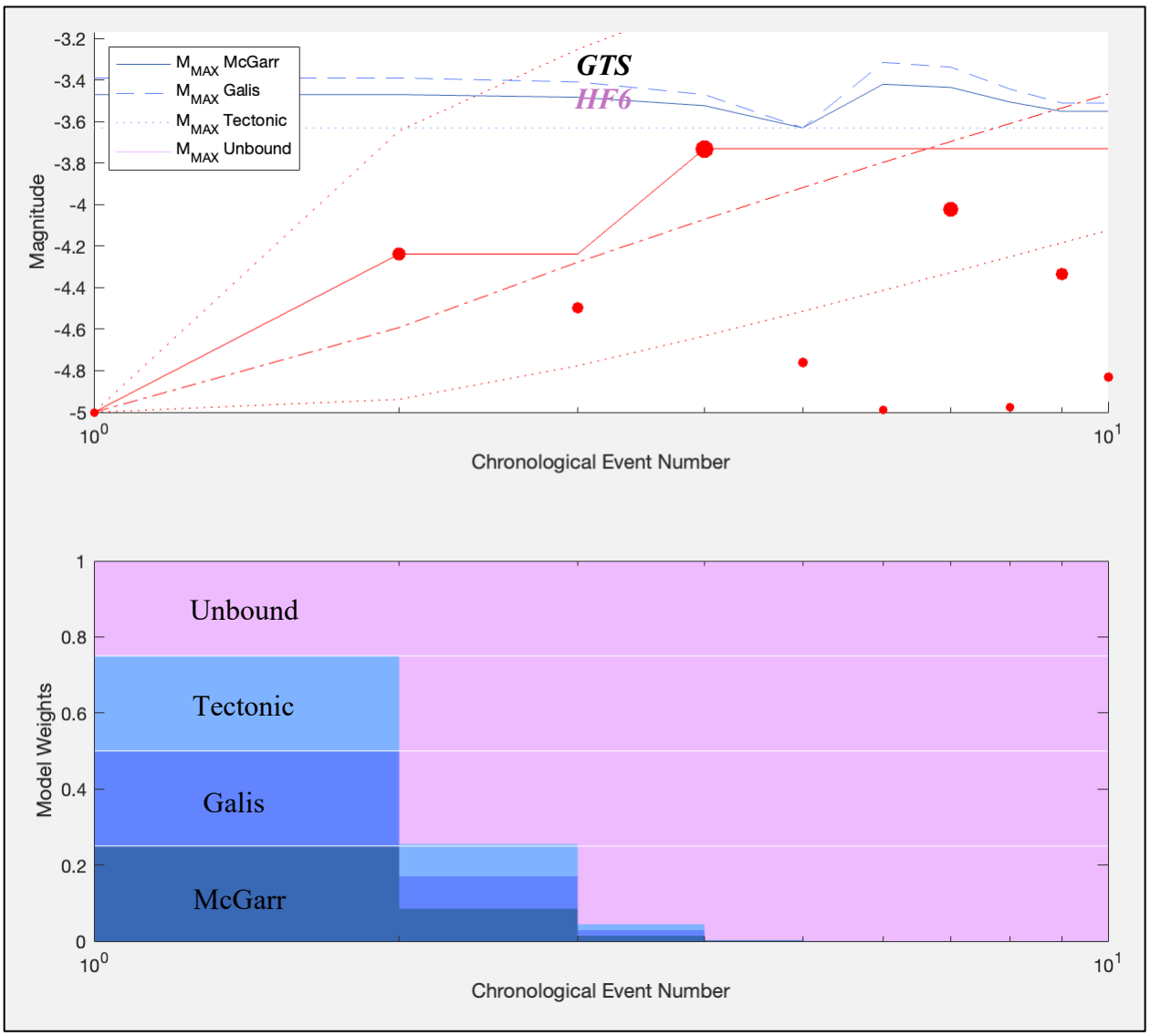

Figure S15. Using the EW-test to discern between M_{MAX} models for HF6 at the GTS. In the top panel, the catalogue of earthquake magnitudes (red circles), the observed M_{LRG} sequence (red lines & circles), and expected M_{LRG} at the 10/50/90 percentiles (red dashed lines) are tested using three M_{MAX} assumptions (blue lines). In the bottom panel, AIC/BIC-based ensemble model weights (coloured bars) using all data prior to each new event are shown.

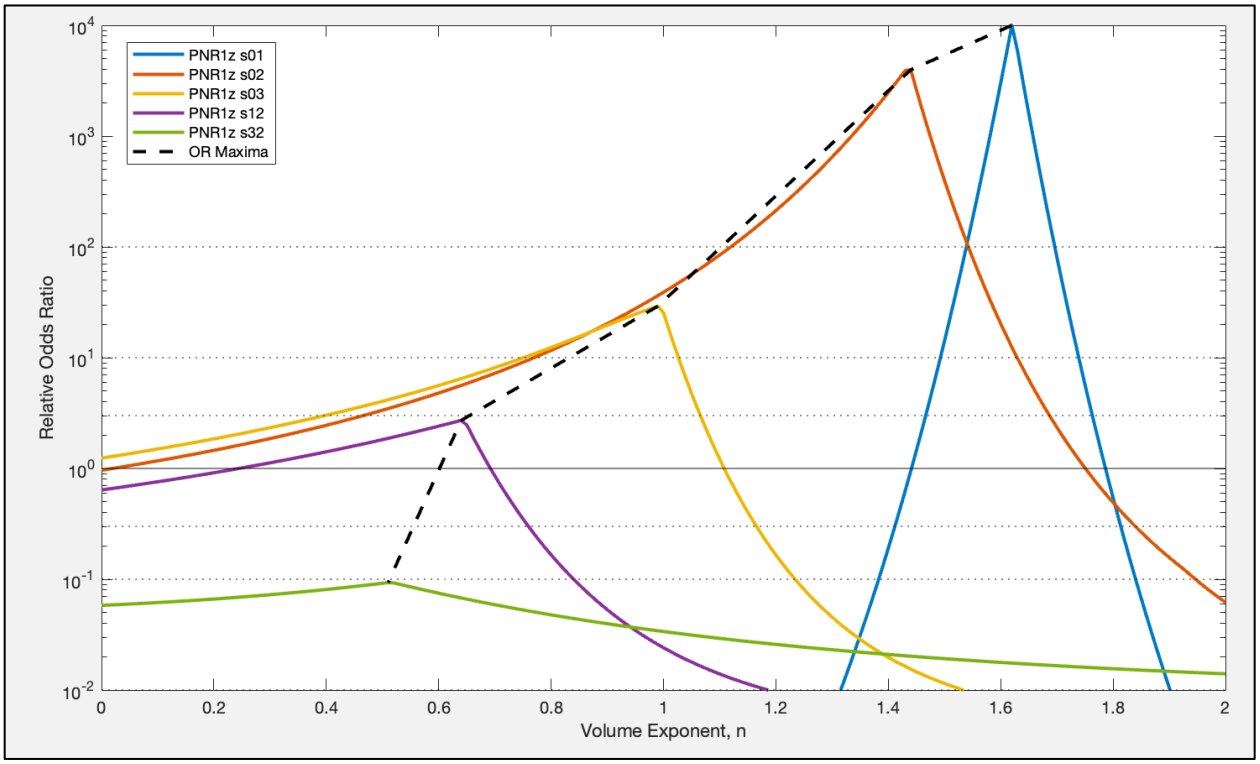

Figure S16. Drop-out test applied to the PNR-1z data. The EW-test is repeated, with initial stages being sequentially omitted. Odds ratios of drop-out clusters (solid lines; relative to the unbound null hypothesis) are plotted alongside statistical confidence thresholds (horizontal dotte lines). The trend of relative odds ratio maxima, as a function of drop-out stages, is also highlighted (dashed black line). Note that relative odds ratios are capped at 10^4 to facilitate an easier comparison via plotting. See also Figure 14b.